

Application of evaporation cooling in a microstructured packed bed reactor for decentralized CO₂ methanation

Sarvenaz Farsi, Shengzhi Liang, Peter Pfeifer, Roland Dittmeyer¹

*Institute of Micro Process Engineering, Karlsruhe Institute of Technology,
Herrmann-von-Helmholz-Platz 1, 76344 Eggenstein-Leopoldshafen, Germany*

Abstract

The objective of this work is the detailed analysis of the performance of an advanced packed-bed reactor with evaporation cooling structure and 1.5 (STP) m³ h⁻¹ reactant throughput. Application of pressurized water as the cooling medium enables stable reactor operation within a safe temperature window at extremely high space-time yield (~ 1000 m³_{CH₄}/m³_{reactor}h, ~ 18000 m³_{CH₄}/m³_{reaction-volume}h). The performance of the reactor regarding its axial temperature profile and product quality under different process conditions such as water coolant flow rate distribution and pressure in cooling passages is evaluated in detail. The feed throughput and composition influence on reactor performance during start-up, steady-state and transient operational conditions for a technical methanation plant are investigated. For reactor description purposes and computing the heat transfer coefficient, a cascade model of perfectly mixed CSTRs is implemented. The modelling results predict the experimental data very well regarding the temperature profile and product composition.}}

Keywords: Power-to-Gas, Decentralization, Evaporation-cooling, Carbon dioxide methanation, Transient operation, Temperature control

1. Introduction

The climate change and its consequences such as increased average and maximum temperatures, extreme weather events and sea-level rise [1] compels collaboration of all energy sectors for development of smart and effective technologies to oppose CO₂ emissions [2].

The methanation reaction of CO₂ and H₂ in the scope of a Power-to-Gas (PtG) technology is one among the many prospects for tackling this issue [3]. A potential scheme of a PtG process is depicted in figure 1. The first step could involve converting the excessive renewable energy from solar or wind power into H₂ through steam electrolysis. The generated H₂ can be either used directly or energetically. At current stage, a widespread H₂ infrastructure as the main energy source is assessed economically infeasible and can be only taken into consideration for special regions with very high H₂ requests [3]. Several projects

work on technical and economical aspects of a H₂ network for both short- and
 15 long-term green H₂ applications [4]. A PtG-H₂ system can be integrated to
 an industrial plant with high H₂ demand such as NH₃ and methanol synthe-
 sis or hydro-cracking. The high renewable power generation potential for such
 locations is a decisive factor in order to provide a continuous H₂ stream. The en-
 20 ergetic implementation of H₂ can be realized via injecting this renewable gas into
 present natural gas lines, which covers a very good and massive infrastructure.
 According to DVGW ¹, apart from methane, CO₂, N₂ and higher hydrocarbons
 (e.g. Propane and Butane), a maximum H₂ concentration of 1.5% can be added
 to the current natural gas pipeline in Germany. Addition of higher H₂ concen-
 25 trations call for detailed evaluation and customization of system components
 [3].

Alternatively, H₂ can be reacted further with CO₂ for CH₄ production and stor-
 age in natural gas grid. Steam can be generated from the highly exothermic
 methanation reaction to supply the steam electrolysis. Several sources of CO₂
 are ahead: industrial plants (such as iron, steel or cement), biogas plants or
 30 air (via direct air capture, DAC) [5]. There is considerable number of research
 articles as well as pilot plant projects proceeding in this field. The detailed
 description of these projects is summarized in [6, 7].

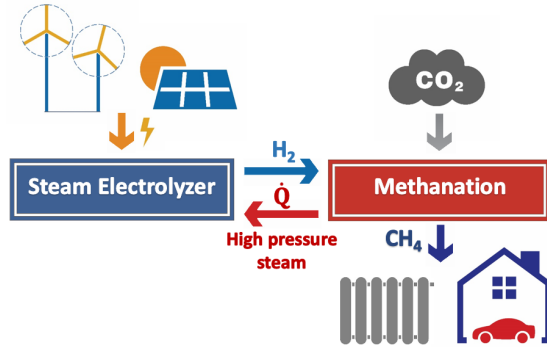


Figure 1: A power-to-Gas (PtG) process scheme: steam electrolysis coupled with methanation of CO₂; reaction heat in methanation as source for steam production.

CO₂ is catalytically hydrogenated according to equation 1. This reaction
 proceeds in two steps as demonstrated in equations 2 (reverse water gas shift
 35 reaction) and 3 (CO methanation). As the reaction enthalpy indicates, it is a
 highly exothermic reaction. A rough estimation serves to grasp the exothermic-
 ity order of magnitude. The theoretical adiabatic temperature of a gas mixture
 with 20 vol.% CO₂ (H₂/ CO₂ = 4, conversion = 100 %) is around 1000 K. The
 methanation reaction and its reverse reforming reaction both proceed on nickel
 40 catalysts. Thus, governed by thermodynamics, temperature window must be

¹The German association for gas and water.

confined in the range of 300-500 °C to hinder the reformation reaction and preserve the catalyst integrity (i.e. avoid catalyst deactivation due to sintering or coke formation) [8, 9]. These obligations, point out the essential challenge for design of methanation reactors and emphasize the development of a smart cooling strategy for the methanation reaction.



The state-of-the-art methanation reactors with respect to heat removal are divided in three major types: 1. the adiabatic fixed-bed reactors (e.g. a cascade of fixed bed reactors with intermediate cooling stages [10]), 2. the isothermal reactors (e.g. fluidized bed reactors [11]) and 3. polytropic reactors [6].

The third class of methanation reactors which combine advantages of high reaction rate and good temperature control are realized via designing coated structured reactors. Honey-comb reactors [12], reactors filled with structured foams [13, 14] and micro-channel reactors [15, 16, 17, 18] can be operated in milder temperatures compared to adiabatic reactors (below 500 °C) and provide an enhanced heat removal. Although coated structured reactors offer superior properties regarding heat transfer and pressure drop, the low amount of catalyst that can be inserted via coating in the reactor imposes larger reactors with high manufacturing costs. The coating process on its own is a challenging task. In case of catalyst deactivation, the reactor might need to be replaced.

Neubert et al. [19] suggested a new methanation reactor with heat pipe integration into a structured reactor. Their initial experimental tests confirmed that in a 5 kW prototype, the hotspot temperature can be well controlled. Extending the process via a second stage fixed bed reactor showed promising product quality for injection in SNG grid. Based on CFD Simulations, Alarcon et al. [20] proposed a reactor applying a multi-tabular design for achieving a high methane yield in elevated space velocities. It was shown that in order to lower the hotspot temperature and operate in thermodynamically controlled reaction regime, the reacting media must be cooled via a cooling media of medium temperature. In the optimal design suggested by Alarcon et al., 1000 tubes were necessary for a medium-size biogas plant.

Giglio et al. [21] studied the optimized reactor parameters, plant efficiency and SNG quality when coupling a high temperature electrolyzer with a methane generation unit. Their work showed that thermal management is the main hurdle in design of the multi-tube fixed bed methanation reactor although having very high heat transfer coefficients when using evaporation of water as the cooling system. Optimization of the methanation unit (e.g. number of the fixed bed tubes, the water coolant temperature and CO₂ flow inlet) had to fulfil several constraints such as the maximum reaction temperature (<550 °C) and outlet CH₄ concentration (95%). The process simulations showed that via integration of the optimized methanation unit and the electrolyzer, an efficiency of 86%

(HHV ²-based) is realizable.

85 Dynamic studies on the catalytic methanation have also caught great attention recently. Dynamics are important in a PtG process due to the fluctuating nature of renewable power and thus the hydrogen. Most of the literature studies are dedicated to modelling and simulation of different types of fixed bed reactors [22, 23, 24]. For instance, dynamic simulations of Li et al. [25] showed that
90 a cooled fixed bed reactor with material and thermal recycle requires up to 1 hour of equilibration in case of imposing step changes of only 2 mol.% in CO concentration in the feed. Lately, Fischer et al. [26] introduced a methodology for designing dynamically operated, load flexible wall-cooled fixed bed tubular reactors. In their approach, the most critical aspects for dynamic operation of
95 a CO₂ methanation fixed bed reactor were already taken into account in the design stage.

Experimental work of Matthischke et al. [27] showed that for having a high CO₂ conversion and temperature control under transient load changes, product recirculation must be adapted. In the research work published by Lefebvre et al.
100 [28] on a three phase bubble column reactor, the step changes in feed velocity caused no fluctuations in the reactor temperature, guaranteed by the good heat removal characteristics of a bubble column. However, since the reaction did not approach equilibrium, the transient conditions changed the product quality. Microstructured technology is one of the most appealing concepts to achieve the
105 target of going one step beyond conventional systems as already shown by the approach of coated structured reactors. The straightforward scale-up strategy in microstructured reactors by numbering-up is another factor in favour for their implementation [29].

The previous studies of Belimov et al. was dedicated to development of a novel
110 microstructured packed bed reactor for the methanation reaction of CO and CO₂ based on specifications prescribed in the MINERVE project. Two reactor prototypes with cooling structure parallel to the catalyst bed were developed. The results of comprehensive experimental work of Belimov et al. on the first prototype are reported in [9]. The prototype consisted basically of a co-feed
115 of coolant and reactive gases. They indicated that water entering the cooling zone at the inlet of the reactor led to a reaction blow out, when the overall heat capacity was reaching the required value. Application of heating cartridges were necessary in order to stabilize the reaction. Through investigations led to the second prototype [30], which is investigated in the current work. A process
120 analysis is provided with a scale-up of this prototype in [31].

The current work focuses on detailed investigations on the second heat exchanger-reactor prototype with regard to the evaporation process which is required in a process scheme according to figure 1. The simple and compact design of the reactor guarantees its scale-up via the numbering-up approach. In contrast to
125 established fixed bed reactors, moderate temperature profiles were achieved, owing to the enhanced cooling strategy. The reactor showed an impressive de-

²Higher heating value.

gree of freedom in adjusting a desirable temperature profile. The ultra-compact micro packed-bed reactor enables stable operation at exceptionally high space time yield ($\sim 1000 \text{ m}^3_{\text{CH}_4}/\text{m}^3_{\text{reactor h}}$, $\sim 18000 \text{ m}^3_{\text{CH}_4}/\text{m}^3_{\text{reaction-volume h}}$) while performing in the ideal temperature window of 300 to 500 °C. The influence of reactor load and composition variation on a Ni-based catalyst is applied. The performance of the reactor under different modes of operation such as start-up, steady-state and transient conditions is analyzed. To assess the reactor behaviour, supply of pressurized water to the cooling structures with varied pressure and in different amount and distribution between two coolant inlets is investigated. Finally, step changes in the reactor throughput and composition are induced in order to asses the reactor degree of stability and response time under transient operational conditions. It was shown that the reactor has a notably fast response time to feed fluctuations owing to its effective thermal management system. Finally, a heterogeneous reactor model based on a one-dimensional cascade of ideally mixed reactors was developed. Special attention is dedicated to the local heat transfer coefficient between the catalytic bed and the cooling channel.

2. Materials and methods

2.1. Microstructured reactor with internal cooling structure

The general reactor concept used in this work is shown in [9, 30] and is illustrated in figure 2. The reactor prototype has two parallel reaction slits with a length of 100 mm, width of 50 mm and height of 2 mm. In between the reaction chambers five holes are manufactured for insertion of heating cartridges. Each heating cartridge was controlled via an adjacent thermocouple, placed in a hole with a diameter of 1 mm. The thermocouples are assigned as **positions 1 to 5**, as depicted in figure 2 (P1 to P5). The main function of heating cartridges is pre-heating the reactor to the reaction temperature and in-situ catalyst reduction via a defined temperature program.

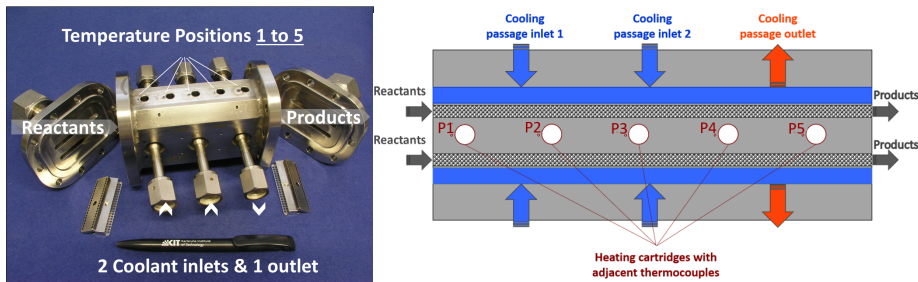


Figure 2: left: The microstructured reactor with two cooling inlets and one common outlet, right: the schematic cross-sectional view of the reactor

The optimization in contrast to the first prototype (see [9]) is the coolant injection via two inlets and one common outlet. The cooling channels constructed

parallel to the catalytic bed compose of 69 rectangular channels of 500 x 500 μm are identical to prototype 1. The added second inlet is aiming to increase the flexibility and potential regarding coolant adjustment. It helps to cool the hotspot local and adjust the coolant flow rate respective to its position. The symmetrical configuration of the reactor with cooling channels on the outer wall grants the assumption that thermocouples inserted along the reaction axis measure the maximum radial temperature in the reactor. This assumption is cross-checked via inserting a thermocouple directly inside the catalyst bed (discussed in section 3.1). In order to minimize heat losses to the environment, the reactor is placed in an aluminium box filled with Microtherm Free flow[®] micro porous insulation granules.

2.2. Experimental setup

The flow chart of the test rig for methanation experiments with integrated evaporation cooling is shown in figure 3. The setup can be divided in 4 sections: I. gas supply, II. microstructured reactor, III. analytics, and IV. the cooling facilities.

- I. The gases CO_2 , H_2 and N_2 were regulated by MKS Instruments mass flow controllers. The reactants were preheated before entering the reactor to 300 °C via heating pipelines. The pipelines leading the products to gas chromatograph (GC) were set to 200 °C to avoid water condensation.
- II. The catalyst inside the reactor was fixed via glass wool and a perforated metal plate which allows homogeneous flow distribution in the reaction passage. Pressure regulation was done using a Flow-Serve[®] needle valve. Pressure drop in the bed was measured via a pressure difference sensor. Temperature of the reactants at the catalytic bed outlet was measured using a thermocouple inserted in the reactor outlet flange. In addition, a thermocouple measured the temperature directly inside the catalytic bed, inserted through the inlet flange.
- III. The product gas was injected into an online GC from Agilent 6890, equipped with two columns and two detectors; HP-Plot Q and HP-Molesieve. The concentration determination in the GC was done via two detectors; a thermal conductivity detector (TCD) for H_2 , N_2 and H_2O analysis and a flame ionization detector (FID) equipped with a Ni catalyst cell for precise CO_2 , CO and CH_4 concentration determination. The data from the online GC was used to calculate CO_2 conversion, selectivity to CH_4 formation and CH_4 yield [32]. A LabView program was applied for saving all the temperature and pressure data continuously throughout the operation.
- IV. Two HPLC pumps from Knauer K-1800 fed the water separately to the cooling passage one and two. The pressure on the coolant side was created using a Swagelok back-pressure regulator, a double-ended Swagelok expansion cylinder and supplying small amounts of N_2 after condensation

200 of the generated steam. The back-pressure regulator cared for a constant
 pressure at its own inlet (before the device itself) and when the pressure on
 the cooling channel streamline surpasses that of the setpoint, the excessive
 flow was released throughout the valve and directed toward the exhaust.
 The temperature of the cooling water before entering the reactor was set
 205 to slightly below its boiling point (2 to 5 K) at the desired pressure. For
 preheating the water, two set of micro heat-exchangers built at our institute
 with 15 heating cartridges 225 W each, followed with heated pipelines
 were installed. The coolant temperature at the inlet and outlet of the three
 cooling channels were controlled using a thermocouple placed directly inside
 210 the inlet or outlet. The generated steam was condensed in a double
 tube heat exchanger with cold water flowing in the outer tube. The expansion
 cylinder was emptied between experiments from the condensed and
 collected water.

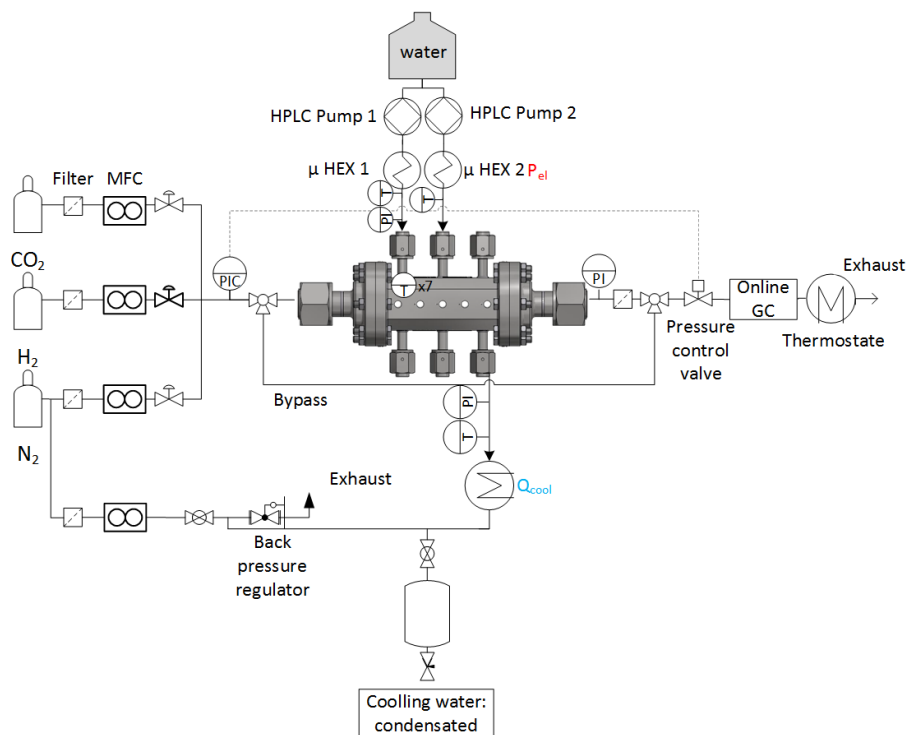


Figure 3: Schematic drawing of the evaporation-cooling methanation test rig.

2.3. Experimental procedure

215 In all experiments, the reactor was filled with 5 g catalyst in the particle
 size of 400-500 μm mixed with 22 g washed, dried and fractioned silicon carbide
 (SiC) in 300-400 μm fraction. In order to assure homogeneous distribution

of the catalyst and inert SiC while filling the powder mixture in the reactor, the catalyst and SiC were divided in five equally weighted portions and mixed together carefully. The mixed fractions were filled in the reactor successively
 220 in order to avoid segregation of the particles due to their differing physical properties (e.g. density and particle size). The investigations were conducted on a with CeO₂ promoted Ni/Al₂O₃ catalyst. The details regarding the catalyst characteristics are not mentioned due to confidentiality reasons. The catalyst was provided in oxidized form and therefore the first step was the catalyst
 225 reduction. The catalyst was reduced online by heating up to 450 °C with a temperature ramp of 2 K min⁻¹ under a mixture of 10% H₂ and N₂ (rest). At 450 °C, the flow was switched to pure H₂ and kept for five hours. When the reduction procedure was completed, the reactor temperature was set to 300 °C and the reactor was flushed with 1 l min⁻¹ (STP) flow of N₂:H₂ (= 1:1). This
 230 temperature and gas mixture were preserved in between the experiments and during standby in order to prevent the catalyst from oxidation. The reaction was always initiated at 300 °C in the absence of cooling water. The N₂ amount was kept equal to 5 vol.% in all experimental runs and acted as the internal standard for product flow rate calculation. With inducing CO₂ in the
 235 gas mixture the reaction initiated immediately. Water pumps were started after surpassing a hotspot temperature of 370 °C. The range of the studied experimental parameters are given in table 1. The reactor was conceptualized for a maximum absolute pressure of 6 bar (at 450 °C) in the reaction zone. Therefore, the reaction pressure was kept constant at this
 240 value during all measurements. The cooling channels were designed for higher pressure, thus the water pressure was raised up to 20 bar.

Table 1: Investigated range of operational conditions in the evaporation cooling reactor.

Experimental parameter	Studied range
Volumetric flow rate (STP)[l min ⁻¹]	10-24
H ₂ /CO ₂ ratio [-]	3-6
Water pressure [bar]	5-20
Water mass flow rate [g min ⁻¹]	2.5-15

The reference measurement point had the operation parameters of H₂/CO₂ ratio of 4, volumetric flow rate of 21.1 (STP) l min⁻¹ (WHSV_{CO₂} = 95 h⁻¹) and was cooled with water cooling pressure of 10 bar (pre-heated to 180 °C). This
 245 reference point was used to judge possible catalyst deactivation during the experiments. Each experiment has been carried out for a minimum of two hours and the product composition and temperature profiles are reported by averaging the collected data after stabilization of the reaction (approximately 30 minutes after reaction start).
 250 In sets of experiments, step changes in the feed throughput with constant feed composition as well as step changes in the feed composition at constant flow were executed and the reactor response time with regard to temperature profile development and product composition was monitored.

Several error sources can affect the results of laboratory data. For example, presence of small fractions of vapour or water drops in the cooling microchannels can affect the startup behaviour of the reactor. Since the reactor operated mainly in thermodynamic regime and the methanation reaction is greatly temperature dependent, modest variations in gas dosage alter the product composition. The calibration margins for each mass flow controller were kept at $\pm 5\%$ (relative error). A thermodynamic analysis for the temperature window of interest and range of reactants compositions was done to assess the possible effect of two hypothetical cases where the reacting CO_2 was dosed below or above its setpoint. This analysis revealed that deviations in dosing CO_2 on the verge of upper/lower uncertainty limits of the CO_2 mass flow controller, can alter the CO_2 conversion degree in an order of $90\% \pm 3\%$.

2.4. Mathematical methods

In this work, the conservation equations in a fixed bed reactor for steady-state conditions were written representing a series of continuously stirred tank reactors (CSTRs). In this approach, a catalytic packed bed reactor is divided in n ideally mixed cells, in which the outlet of each cell serves as the inlet for the next cell. The model considers no back-mixing between the adjacent cells. The interaction between the solid and gas phase is specified via reaction and diffusion. The gas phase is assumed as ideal gas. The energy and mass balances are coupled and solved simultaneously. The pressure drop is considered negligible, therefore no momentum balance is solved. The axial mass dispersion and thermal heat conduction (dissipation) is hooked implicitly into the model via adjusting the number of cells. Estimation of the Carberry number showed that the external mass transfer resistances in the catalytic bed are not considered relevant. External heat transfer calculations according to Mears criterion referred to some degree of film over-heating which was considered tolerable for the reactor modelling purposes. Comparable results were achieved in the PhD work of Belimov for methanation of CO/CO_2 mixtures, which has an even higher reaction rate and exothermicity degree [33]. Therefore, the conditions (i.e. temperature and concentration) at the surface of the catalyst are identical to those in the bulk phase in a specific cell.

The mass and energy balance in the solid spherical catalyst pellets can be written as:

$$D_{i,eff} \left(\frac{2}{r} \frac{dC_i}{dr} + \frac{d^2 C_i}{dr^2} \right) = \rho_{cat} \cdot R_i(C_i, T) \quad (4)$$

$$\lambda_{eff} \left(\frac{2}{r} \frac{dT}{dr} + \frac{d^2 T}{dr^2} \right) = -\rho_{cat} \cdot R_i(C_i, T) \cdot (-\Delta_R H) \quad (5)$$

where $D_{i,eff}$ is the effective diffusivity of species i in the reaction mixture, which was determined using the Bosanquet diffusion model [34]. The λ_{eff} represents the effective thermal conductivity in a solid particle. The concentration and temperature in the bulk phase are the boundary conditions for the catalyst particle. The second boundary condition imposes zero gradient of temperature

and concentration in the center of the catalyst (the symmetry condition).

$$\left. \frac{dC_i}{dr} \right|_{r=0} = 0 \quad \text{and} \quad C_i \Big|_{r=R} = C_{i,surface} \quad (6)$$

295

$$\left. \frac{dT}{dr} \right|_{r=0} = 0 \quad \text{and} \quad T \Big|_{r=R} = T_{surface} \quad (7)$$

Each cell is modelled as a well-mixed CSTR. Therefore, the conservation of mass and energy for each cell with a length of Δx and for the bulk phase can be written in the form of the following algebraic equations:

$$u_x \cdot C_{i,x} \cdot A_{cross} + J_M \cdot \Delta S_{cat} = u_{x+dx} \cdot C_{i,x+dx} \cdot A_{cross} \quad (8)$$

$$\dot{m} \cdot C_{p,x+dx} \cdot T_{x+dx} - \dot{m} \cdot C_{p,x} T_x + \Delta A_{cool} \cdot k_{eff} \cdot (T_{x+dx} - T_{cool}) = \dot{Q}_{reac.} \quad (9)$$

300

The parameters ΔA_{cool} and ΔS_{cat} represent the cooling area and catalyst surface area in one control volume, respectively. k_{eff} corresponds to the overall heat transfer coefficient. The heat of the reaction is defined as:

$$\dot{Q}_{reac.} = dm_{cat} \sum_j (-\Delta_R H_j) \cdot R_j \quad (10)$$

305

The overall heat transfer coefficient can be calculated having the heat duty of the system, the area of the heat exchange and the temperature difference between the two reactor zones, as the following equation:

$$\dot{Q} = k_{eff} A_{cool} (T(x) - T_c) \quad (11)$$

310

For simplicity in estimation of the k_{eff} using equation 11, the temperature of water coolant (T_c) was assumed to remain constant along the channel and equal to the evaporation temperature at the respective pressure. For approximation of the axial temperature profile in the reactor ($T(x)$), 6 experimentally measured points were used: the temperature at the entrance (pre-heating temperature), 4 temperature measurement positions and the reactor outlet temperature. A cubic spline function was used for interpolation of the temperature in each cell, based on these experimental axial temperature points. This estimated temperature was inserted as $T(x)$ in equation 11. The numerical computation of the concentration and temperature change in the catalyst particles is a boundary value problem and was done via `bvp4c` solver in Matlab[®]. The catalyst was discretized in 50 grid cells. The reactor was divided in 100 CSTR cells. For the case of catalyst particles, the number of the grid cells was set to the value, which further increase in the number of cells showed no effect on the results. The number of the CSTR cells was calculated based on the Bodenstein number as described in the reference book [35]

320

For cubic spline interpolation of the axial temperature profiles in the reactor based on experimental data points, `csapi` Matlab function was used. The starting temperature was constrained to 300 °C. The `fnval` function was implemented for evaluating the computed values from the temperature fit for each

325

cell.

The reaction kinetic model applied here describes CO₂ methanation as a two-step reaction taken from [32], and are formulated as follows:

$$r_{rWGS} = \frac{k_{rWGS} p_{CO_2}^{0.5} p_{H_2}^{0.5}}{(1 + K_{H_2O} p_{H_2O})^2} \cdot \left(1 - \frac{p_{CO} p_{H_2O}}{p_{CO_2} p_{H_2} K_{eq.,rWGS}}\right) \quad (12)$$

$$r_{CO-methanation} = \frac{k_{CO-meth.} p_{CO} p_{H_2}^{0.5}}{(1 + K_{H_2O} p_{H_2O})^2} \cdot \left(1 - \frac{p_{CH_4} p_{H_2O} p_{abs.}^2}{p_{CO} p_{H_2}^3 K_{eq.,CO-meth.}}\right) \quad (13)$$

330 3. Results and discussion

3.1. Reactor start-up

The start-up behaviour of the reactor and its response time to water dosage is evaluated at the reference measurement point (see section 2.3). In figure 4 the temperature development along the catalyst bed axis during reactor start-up and until reaching steady-state conditions is presented.

335

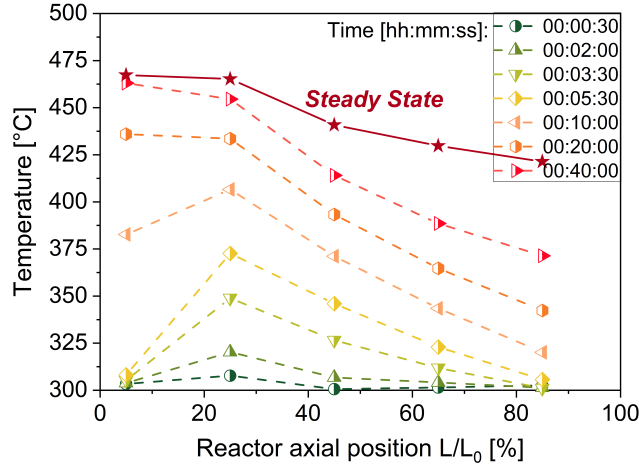


Figure 4: Reactor start-up behavior ($\dot{V}_{tot} = 21.1 \text{ l min}^{-1}$, $H_2/CO_2 = 4$, $p_w = 10 \text{ bar}$, $\dot{m}_{w,1} = 9.5 \text{ g/min}$ and $\dot{m}_{w,2} = 1.0 \text{ g/min}$)

After 30 seconds of dosing CO₂, temperature starts to rise in the second temperature measurement position, with a clear tendency to form a hotspot in this position only after three minutes. The rate of temperature rise in position 2 is about 10 K min^{-1} and has the highest growth rate. The slowest temperature increase rate is at position 5 with only 2 K min^{-1} . The temperature growth in position 1 is rather different. The heating cartridge in this position continues to consume electricity for around 10 minutes after reaction initiation. Therefore, position 1 is the last part of the reactor in which the reaction starts. After

340

345 this initial delay, temperature starts to increase in position 1 and reaches an identical value as position 2 within 20 minutes. The temperature in positions 3 to 5 develop very slowly in comparison. Nevertheless this is a continuous trend and tends to decrease the temperature gradient along the bed.

The HPLC water pumps are started after about 8 minutes of reaction run time. In order to avoid reaction blow out, the water flow rates are set first to small 350 values (1-3 g/min) and are increased gradually to keep the hotspot temperature below the desired value. After about 20 minutes, the temperature profile approaches 'quasi steady-state' conditions. Slight adjustments in the water flow rate (0.5-1 g/min) were necessary in order to retain the temperature stable. The steady-state profile in figure 4 is reached with adjusting 9.5 g/min water 355 in water inlet 1 and 1.0 g/min in water inlet 2. The temperature difference between the first and fifth position in the steady-state condition is about 45 K, and between position 1 and 3 is about 20 K. This experiment shows that despite the remarkably high cooling efficiency of evaporation cooling, temperature gradients along the reactor axis cannot be avoided. Due to the extreme reac- 360 tion heat release at the front part and fast kinetics the temperature at the front is higher and decreases monotonically in the second half of the reactor. This effect is discussed in detail in section 3.2. Hence, with slight water flow control in pressurized evaporation cooling, the typical sharp methanation hotspot is mitigated and a moderate temperature profile governs along the catalytic 365 bed. Most importantly, the difficulties experienced by Belimov et al. during evaporation cooling in reactor prototype 1 are avoided in the reactor prototype 2: no reaction blow out or runaway are encountered and the reactor performs autothermal. The measured CO₂ conversion at the reactor outlet was about 90% and the selectivity to methane was over 99% for this experiment.

370 In order to assure that the temperatures measured from the central metal block are not delayed by the heat conductivity characteristics of the catalyst bed and the high heat capacity of the metal, a thermocouple was inserted directly inside the catalyst bed between position 2 and position 3. Figure 5-left shows the development of the temperature in positions 2 and 3 and the catalyst bed in 375 the first 10 minutes of reaction. Similar to observations of Belimov et al. [9], the temperature in the catalyst bed in the first 5 minutes is slightly higher than positions 2 and 3. However, the maximum temperature difference is less than 25 K and thus less than the 80 K reported by Belimov et al. under CO/CO₂ conditions. The presence of CO seems to accelerate the hotspot formation. The growth rate in catalyst bed in the first 5 minutes is 16.8 K min⁻¹, whereas this 380 value for position 2 and 3 is 14.5 K min⁻¹, and 9.2 K min⁻¹, respectively. At the 6th minute, the temperature in position 2 and catalyst bed overlap and shortly after, it drops further down and lays perfectly between positions 2 and 3. The temperature growth rate diminishes considerably after dosing coolant water (TOS = 10 min) and serves to be 3 K min⁻¹ for position 2 and the catalyst 385 bed and 2 K min⁻¹ for position 3.

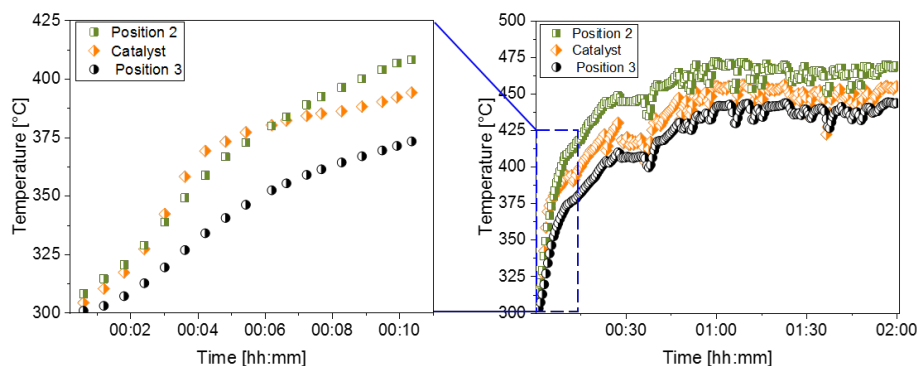


Figure 5: Comparison of the temperature development in the catalyst bed and in the metal bulk. Left: during the first 10 min of reactor start-up, right: for two hours of operation ($\dot{V}_{\text{tot}} = 21.1 \text{ l min}^{-1}$, $\text{H}_2/\text{CO}_2 = 4$, $p_w = 10 \text{ bar}$, $\dot{m}_{w,1} = 9.5 \text{ g/min}$ and $\dot{m}_{w,2} = 1.0 \text{ g/min}$)

Figure 5-right depicts the temperature development in the three aforementioned positions during two hours of run time. The dynamic reaction nature through evaporation cooling is clearly resolved via numerous scattered temperature measurements throughout the time. The drops and rises in the temperature may also be a result of HPLC pump pulsations. Additionally, The intensity of these fluctuations depends on operational parameters, e.g. the coolant inlet temperature. This issue is discussed in detail in section 3.3.

3.2. Temperature profile optimization

In the following section, the reactor degree of flexibility regarding temperature regulation and the influence of water flow rate in each cooling passage on the temperature profile is discussed. The pressure of water is kept at 10 bar and temperature of water at reactor inlet is adjusted to 175-180 °C accordingly. The reactants flow rate and composition are kept at reference condition (see section 2.3). The relevant information which will be discussed in detail in the following is: The cooling passage 1 controls the temperature in positions 1 and 2, further called **front** reactor part. Whereas cooling passage 2 affects the temperature in positions 3 to 5, further called **rear** reactor part.

Temperature manipulation by shifting water flow from water inlet 1 to inlet 2:

From experiment P2-test 1 to P2-test 4 ($\dot{V}_{\text{tot}} = 21.1 \text{ l min}^{-1}$, $\text{H}_2/\text{CO}_2 = 4$, $p_w = 10 \text{ bar}$, water flow rates according to table 2) the cooling potential is gradually shifted to the second water inlet. Table 2 presents the amount and distribution of water in each cooling channel, the temperature of steam in reactor outlet, the degree of CO_2 conversion, CH_4 selectivity and yield of CH_4 production for the mentioned experiments. In this set of experiments, the temperature of the hotspot at position 2 was constant at 440 °C and temperature in positions 3 to 5 varied (figure 6-left).

In experiment P2-test 1, coolant is mainly dosed in the cooling inlet 1, and the water flow rate is set to a minimum value of 1 g min^{-1} . It was observed that by

complete elimination of the second pump, the hotspot temperature escalates. Therefore, during all measurements, both pumps are turned on and the flow of pump 2 was further set to a minimum of $\sim 0.5 \text{ g min}^{-1}$.

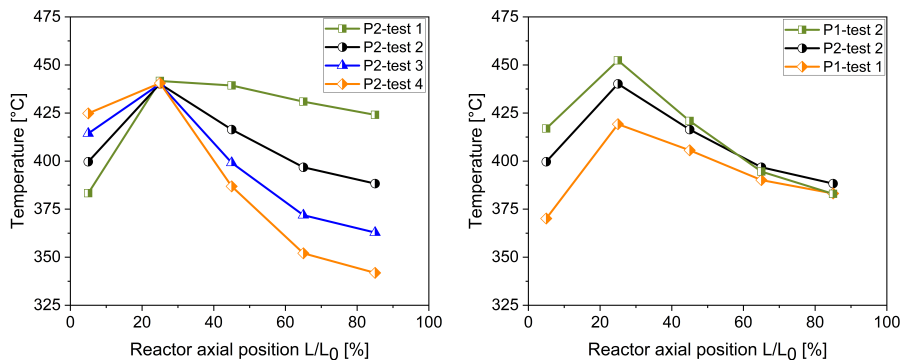


Figure 6: Steady-state temperature profiles. Left: rear reactor part experiment, right: front reactor part experiment ($\dot{V}_{\text{tot}} = 21.1 \text{ l min}^{-1}$, $\text{H}_2/\text{CO}_2 = 4$, $p_w = 10 \text{ bar}$, water flow rates according to table 2 and 3).

420 Although the total mass flow rate of water was slightly increasing in this P2-test series, it is obvious from experiment P2-test 2, P2-test 3 and P2-test 4 that increasing the coolant in passage 2 and simultaneous decreasing the water flow rate in passage 1 retains the hotspot at the same level. This leads to the conclusion that the water mass flow at inlet 1 has almost no impact on controlling the hotspot at position 2. This is similar to observations of Belimov
 425 et al. [9], which conclude that this is most probably due to a heat transfer limitation by the wall thickness separating cooling media and catalyst. The strategy to shift the water flow to inlet 2 is, however, at the expense of increasing the temperature gradient between the front and rear reactor part.

430 An interesting observation is that, in experiment P2-test 1, where the coolant in second pump is set to only 1 g min^{-1} , the temperature difference between position 2 and 5 is only 16 K. i.e., when water is applied only in the first 20% of the reactor length, the temperature in the rest of the reactor remain almost constant. This suggests that the water mainly evaporates in the front reactor part, as the reaction is at equilibrium in all cases at the reactor outlet. This in
 435 turn implies that a part of the reactor rear is not used for reaction. We assume that the good heat conductivity characteristics of the central metal block also play an important role. The high temperature in the front part of the metal block compared to rear part results in a considerable heat flux. Thus, the metal block indirectly reduces the axial gradient in the packed bed.

Table 2: Temperature variation by shifting coolant flow from inlet 1 to 2: the coolant amount, outlet temperature, product ($\dot{V}_{\text{tot}} = 21.1 \text{ l min}^{-1}$, $\text{H}_2/\text{CO}_2 = 4$, $p_w = 10 \text{ bar}$)

Experiment label	$\dot{m}_{w,1}$ [g min ⁻¹]	$\dot{m}_{w,2}$ [g min ⁻¹]	$\Sigma\dot{m}_w$ [g min ⁻¹]	$T_{w,\text{outlet}}$ [°C]	X_{CO_2} [-]	S_{CH_4} [-]	Y_{CH_4} [-]
P2-test 1	10.5	1.0	11.5	280	92.7%	99.8%	92.6%
P2-test 2	6.2	6.5	12.7	261	93.0%	99.9%	92.9%
P2-test 3	2.8	10.2	13.0	255	92.3%	99.9%	92.2%
P2-test 4	0.3	12.7	13.0	238	91.0%	99.9%	90.8%

440 **Temperature manipulation of the hotspot:**

In this set of experiments (P1-test 1, P1-test 2 and P2-test2), we manipulated the hotspot temperature as far as possible from heat transfer limitation point of view by keeping the flow rate of water at inlet 2 and thus the temperature in the reactor rear near constant and the cooling potential is gradually shifted to the second water inlet ($\dot{V}_{\text{tot}} = 21.1 \text{ l min}^{-1}$, $\text{H}_2/\text{CO}_2 = 4$, $p_w = 10 \text{ bar}$, water flow rates according to table 3). Figure 6-right and table 3 exhibit the temperature profile results, water flow rates and product composition, respectively.

445 During experiment P1-test 1, the coolant amount in passage 2 is kept near the same value as in P2-test 2 and water flow rate in passage 1 is increased (0.8 g min⁻¹). This increase in coolant leads to 30 K temperature drop in position 1 and 20 K in position 2. The temperature in position 3 also diminishes about 10 K. Thus, varying the coolant in one passage, without any effect on other reactor parts is impossible.

450 The lowest possible hotspot temperature, i.e. without blowing out the reaction was 410 °C and was obtained at P1-test 1. At this point, it must be emphasized that this limit is only valid for the current operational parameter. Enhancing the water pressure, i.e. reduction of temperature gradient between coolant and bed, increasing the load, i.e. increasing the released reaction heat or changing the reactants composition would directly influence the operational limit and can shift this margin to lower or higher temperatures.

455 The highest hotspot temperature in this experiment series was 455 °C (P1-test 2). In both series it is obvious that the reactor inlet temperature (position 1) is highly responsive to changes in water flow rate and only 1.0 g min⁻¹ increase or decrease can create up to 20 K temperature shift.

460 **Remarks on the conversion and selectivity by manipulation of reactor temperature:**

In a polytropic reactor, the temperature rise in the inlet supports enhanced reaction rates, whereas the final conversion is dependent on the temperature in the rear part. Governed by thermodynamics, usually lower temperatures in the rear section are desired.

470 In experiments P2-test 1 to P2-test 4, the conversion lies between 92 to 93%, and having in mind the experimental error, experiment P2-test 4 has the lowest conversion of 91%. Experimental runs of P1-test 1, P1-test 2 and P2-test 2, all display the same conversion degree despite hotspot temperature difference. The lowest conversion of P2-test 4 suggests that providing a high temperature only

in the front part and a sharp decrease in the rear part is not optimal in the trade off between reaction rate and thermodynamics. Comparison of P2-test 4 with other temperature profiles implies that position 3 (or perhaps even position 4) affects this balance. If the temperature in position 3 is above ~ 400 °C, the conversion seems to better approach the equilibrium.

The methane selectivity for all the experimental runs was above 99.8% and does not require any further discussion. As all points reach high conversion and selectivity, the amount and temperature of the generated steam in the scope of PtG is interesting. Among all, P2-test 1 has the highest steam temperature, which can be correlated with lower amount of water dosed, specially in the second passage. However, due to minimization of the water coolant in channel 2, the possibility of reaction runaway in this operational frame imposes some technical challenge. The second highest coolant temperature is observed in P1-test 1 with 264 °C. This operational point is also not accredited due to operating on the lower temperature limit of the reactor and being prone to reaction blow-out. Therefore, P2-test 2 is selected as the optimal temperature profile with a steam temperature of 261 °C, high CO₂ conversion and a stable temperature profile.

Table 3: Temperature manipulation of the hotspot: the coolant amount and outlet temperature, product ($\dot{V}_{\text{tot}} = 21.1 \text{ l min}^{-1}$, $\text{H}_2/\text{CO}_2 = 4$, $p_w = 10 \text{ bar}$)

Experiment label	$\dot{m}_{w,1}$ [g min ⁻¹]	$\dot{m}_{w,2}$ [g min ⁻¹]	$\Sigma\dot{m}_w$ [g min ⁻¹]	$T_{w,\text{outlet}}$ [°C]	X_{CO_2} [-]	S_{CH_4} [-]	Y_{CH_4} [-]
P1-test 1	7.0	6.5	13.5	264	92.3%	99.9%	92.2%
P1-test 2	3.0	8.9	12.0	255	92.3%	99.9%	92.2%

3.3. Coolant pressure variation

The temperature difference between the cooling medium and the reaction chamber is an important factor which can lead to instabilities in the reaction zone if it is set too high. Three pressures of 5, 10 and 20 bar were tested for the water supply. The aim was to reproduce a comparable temperature profile as the one generated in experiment P2-test 2 (see section 3.2) by means of water flow rate adjustment. Figure 7 presents the steady-state temperature profile for these three water pressures. Table 4 summarizes the water flow rates, steam temperature, and product quality. It is observed that for all three pressures, it is very likely to achieve a steady-state operation with an identical CO₂ conversion, see table 4. The amount of dosed coolant needed to be reduced for about 1.0 g min^{-1} for every 30 K decrease in the water boiling temperature.

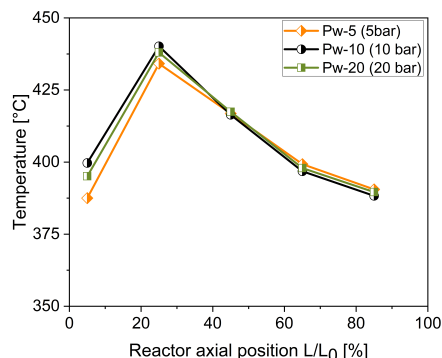


Figure 7: Steady-state temperature profiles in varied water pressure ($\dot{V}_{\text{tot}} = 21.1 \text{ l min}^{-1}$, $\text{H}_2/\text{CO}_2 = 4$, water mass flow rates according to table 4)

505 In section 3.1 it is mentioned that after reaching steady-state conditions, slight changes in the flow rate are required in order to keep the temperature in the desired range. In practice, this was confirmed by the intensity of necessary re-adjustments due to temperature instability. Figure 8 a-c shows all the saved temperature profiles when applying water under 5, 10 and 20 bar, respectively.

510 The presented temperature profiles are collected after reaching 'quasi steady-state' conditions. The parameter of time is brought into image via color palette (green to red). This would help to comprehend if the fluctuations follow a certain trend with time. The black line corresponds to the average value, which is referred as the steady-state profile as also depicted in figure 7. It is evident

515 that the most unstable operation belongs to the experiment with 5 bar water pressure. The range of temperature fluctuations is about 20 K. The amount of dosed water coolant noted in table 4 is the mean dosed water flow rate, plus and minus the range that it was necessary to counteract the temperature changes. The most stable operation is clearly carried out at coolant pressure of 20 bar.

520 Operation at 10 bar behaves not much different from 20 bar and therefore can be considered a good option for further investigations.

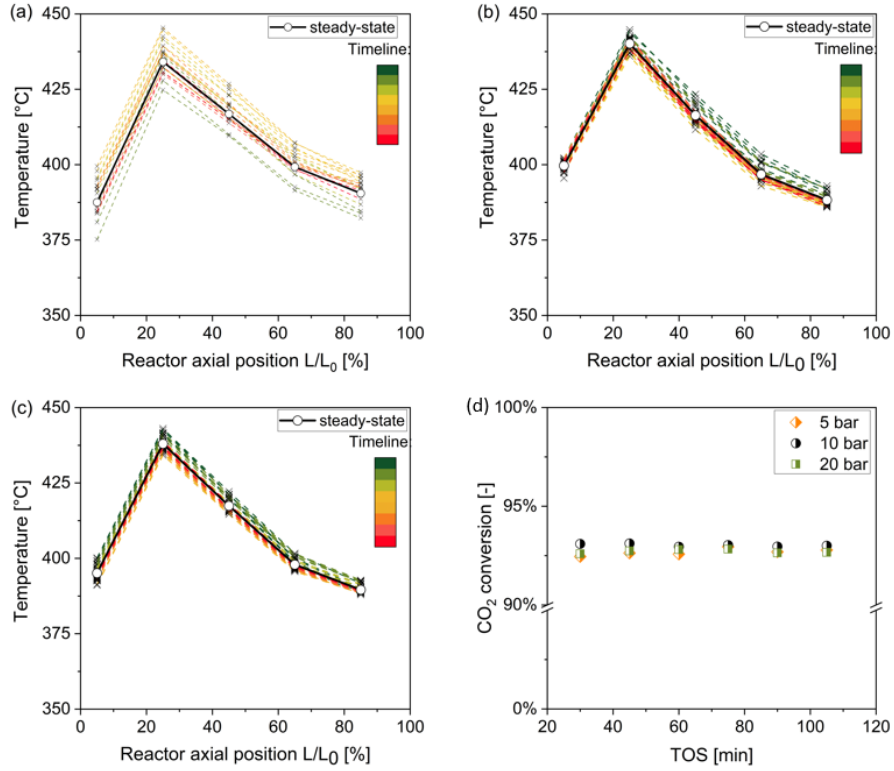


Figure 8: a - c: Influence of the water pressure on temperature profile fluctuation. a: 5 bar, b: 10 bar, c: 20 bar, d: CO₂ conversion for 120 minutes TOS for varied water pressure ($\dot{V}_{\text{tot}} = 21.1 \text{ l min}^{-1}$, $\text{H}_2/\text{CO}_2 = 4$, water mass flow rates according to table 4)

Table 4: Water pressure variation experiment: the coolant amount and outlet temperature, product ($\dot{V}_{\text{tot}} = 21.1 \text{ l min}^{-1}$, $\text{H}_2/\text{CO}_2 = 4$)

Experiment label	$\dot{m}_{w,1}$ [g min ⁻¹]	$\dot{m}_{w,2}$ [g min ⁻¹]	$\Sigma \dot{m}_w$ [g min ⁻¹]	$T_{w,\text{outlet}}$ [°C]	X_{CO_2} [-]	S_{CH_4} [-]	Y_{CH_4} [-]
Pw-5	5.9 ± 0.5	5.7 ± 0.5	11.6	258	92.7%	99.9%	92.6%
Pw-10	6.2 ± 0.2	6.5 ± 0.2	12.7	261	93.0%	99.9%	92.9%
Pw-20	6.7	7.0 ± 0.1	13.7	271	92.6%	99.9%	92.4%

3.4. Load variation

The vol. flow rate of the reactants is varied between 10.6 to 23.7 l min⁻¹ (STP), keeping the H₂/CO₂ ratio and the individual partial pressures constant. Table 5 also shows the dosed coolant in each passage, the temperature of the generated steam, and the conversion degree of CO₂ and CH₄ selectivity and yield. Figure 9-left displays the steady state temperature profiles for the varied feed flow rate. None of the measurements were disturbed due to reaction blow

out or runaway. The distinction between different temperature profiles is the
 530 shift to higher temperatures in the position 1, when the feed flow rate is reduced.
 This shift may be a consequence of the longer residence time of the reactants in
 the reactor, i.e. near full conversion happens directly in the reactor inlet. Via
 individual and proper adjustment of the coolant flow, harsh discrepancy between
 the temperature profiles in the rear reactor part through variation of the feed
 535 flow is evaded. This strategy is important to reach comparable conversions at
 the reactor outlet.

During start-up and absence of coolant, the sudden heat release at higher flow
 rates, promotes the temperature hotspot and generates a great gradient along
 the reactor in short time. Figure 9-right shows temperature profiles after 4
 540 minutes of dosing CO₂ for the different loads. At higher flow rates, the coolant
 potential during the start-up must be immediately concentrated in the first
 passage, while at lower flow rates both passages can be equally started for
 reaching temperature control.

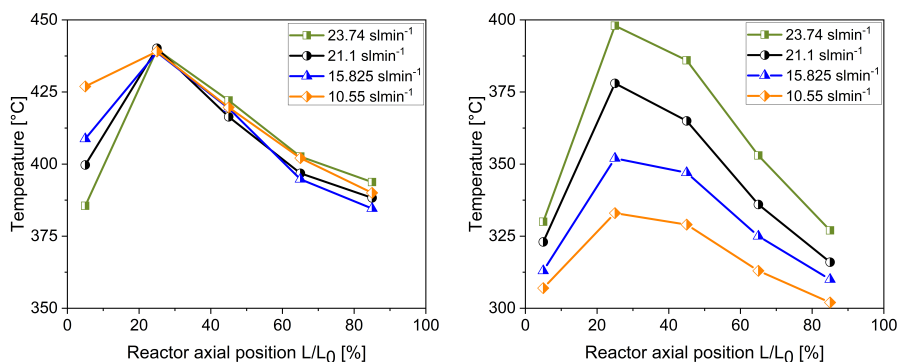


Figure 9: Load variation experiment: left: steady-state temperature profile, right: temperature profile after 4 minutes of reaction initiation ($H_2/CO_2 = 4$, $p_w = 10$ bar, water mass flow rates according to table 5)

The calculated released reaction heat for this throughput range is equal to
 545 245 to 552 W. The removed heat through water temperature increase of 5 K
 and subsequent evaporation for the tested reactant flow rate range is about 91-
 495 W. Considering 30-50 W heat losses as measured by Belimov et al. [9],
 super-heating of the generated steam can be justified. The outlet temperature
 of the steam changes from 273 to 215 °C for various loads. The CO₂ conversion
 550 for the entire range changes between 92.6 % to 94.1 %. The selectivity to CH₄
 formation is also constant and close to 100 %.

Table 5: Load variation experiment: the coolant amount, outlet temperature and reaction parameters ($H_2/CO_2 = 4$, $p_w = 10$ bar, in steady state)

Throughput STP [$l \text{ min}^{-1}$]	$\dot{m}_{w,1}$ [$g \text{ min}^{-1}$]	$\dot{m}_{w,2}$ [$g \text{ min}^{-1}$]	$\Sigma\dot{m}_w$ [$g \text{ min}^{-1}$]	$T_{w,\text{outlet}}$ [$^{\circ}\text{C}$]	X_{CO_2} [-]	S_{CH_4} [-]	Y_{CH_4} [-]
23.7	7.1	7.5	14.6	273	92.6%	99.8%	92.5%
21.1	6.2	6.5	12.7	261	93.0%	99.9%	92.9%
15.8	4.1	3.7	7.8	252	93.3%	99.9%	93.4%
10.6	1.0	1.7	2.7	215	94.1%	99.9%	94.1%

3.5. H_2/CO_2 ratio variation

Two scenarios were followed for studying the effect of H_2/CO_2 ratio variation. In the first scenario, the flow rate of CO_2 was kept constant ($= 3 \text{ l min}^{-1}$) and H_2 flow rate is changed in order to change the H_2/CO_2 ratio between 3 and 6. The second scenario was conducted in constant total flow rate ($= 15.8 \text{ l min}^{-1}$) and altering the H_2 and CO_2 flow rates to meet the desired reactants ratio. For further details please refer to tables 6 and 7. After every experiment with under-stoichiometric H_2/CO_2 ratio, the reference measurement point was repeated to check for possible catalyst deactivation through carbon formation. For this purpose, the CO_2 conversion and the temperature profile was compared to the reference experiment on the fresh catalyst.

$\dot{V}_{CO_2} = \text{const.}$ (scenario 1):

No hint on potential limitations of the reactor to control the temperature in different feed compositions were observed. Only marginal temperature profile differences were measured while an increase in total water mass flow was required to control the reaction at increasing H_2/CO_2 ratio. This demand to increase the water flow was attributed to elevated released reaction heat due to higher CO_2 conversion in excess of H_2 . In the opposite direction, i.e. by decreasing the H_2 flow rate, the CO_2 conversion diminishes and so the released reaction heat. At a stoichiometric ratio of 5 to 6 no further improvement in conversion are found and the unconverted excess of H_2 works in the favour of heat removal. Therefore, less water is needed at $H_2/CO_2=6$ and the steam temperature declines.

Table 6: The H_2/CO_2 ratio variation experiment, scenario 1: the coolant amount and outlet temperature, total volumetric flow rate and product ($\dot{V}_{CO_2} = \text{const.} = 3 \text{ l min}^{-1}$, $p_w = 10$ bar)

H_2/CO_2 ratio	\dot{V}_{tot} [$l \text{ min}^{-1}$]	$\dot{m}_{w,1}$ [$g \text{ min}^{-1}$]	$\dot{m}_{w,2}$ [$g \text{ min}^{-1}$]	$\Sigma\dot{m}_w$ [$g \text{ min}^{-1}$]	$T_{w,\text{outlet}}$ [$^{\circ}\text{C}$]	X_{CO_2} [-]	S_{CH_4} [-]	Y_{CH_4} [-]
3.0	12.7	1.9	2.5	4.4	228	74.4%	99.8%	74.2%
3.5	14.2	3.1	3.0	6.1	240	85.2%	99.8%	85.0%
4.0	15.8	4.1	3.7	7.8	252	93.3%	99.9%	93.1%
5.0	19	3.6	5.0	8.6	250	99.2%	100%	99.2%
6.0	22.2	3.0	5.1	8.1	245	99.7%	100%	99.7%

575 $\dot{V}_{\text{tot}} = \text{const. (scenario 2):}$

Again almost identical temperature profiles were obtained in this series. Regarding the applied coolant a different trend can be noticed for scenario 2 in contrast to scenario 1. In the case of keeping the total feed and hydrogen flow constant, the maximum heat release corresponds to the H_2/CO_2 ratio of 4. This is reflected by the maximum water demand in table 7. By decreasing the H_2/CO_2 ratio, the conversion drops and therefore less water is demanded. In the opposite direction, the over-stoichiometric ratio increases the CO_2 conversion, but since less CO_2 is dosed, the overall released heat is lower and so less cooling is needed. The direct comparison of the steam temperature in reactor outlet confirms this claim.

Another valuable information achieved from comparison of scenario 1 and 2 is the identical CO_2 conversion for these two cases. This measurement supports that the reactor always operates in thermodynamic regime.

Table 7: The H_2/CO_2 ratio variation experiment, scenario 2: the coolant amount and outlet temperature, CO_2 volumetric flow rate and product ($\dot{V}_{\text{tot}} = \text{const.} = 15.81 \text{ min}^{-1}$, $p_w = 10 \text{ bar}$)

H_2/CO_2 ratio	\dot{V}_{CO_2} [l min^{-1}]	$\dot{m}_{w,1}$ [g min^{-1}]	$\dot{m}_{w,2}$ [g min^{-1}]	$\Sigma \dot{m}_w$ [g min^{-1}]	$T_{w,\text{outlet}}$ [$^{\circ}\text{C}$]	X_{CO_2} [-]	S_{CH_4} [-]	Y_{CH_4} [-]
3.0	3.8	3.5	3.7	7.2	241	74.4%	99.8%	74.2%
3.5	3.3	3.8	3.6	7.4	250	84.6%	99.8%	84.5%
4.0	3	4.1	3.7	7.8	252	93.3%	99.9%	93.1%
5.0	2.5	2.5	4.0	6.5	240	99.5%	100%	99.5%
6.0	2.1	1.5	2.1	3.6	213	99.9%	100%	99.9%

3.6. Measures of reactor stability under transient operation

590 3.6.1. Load step changes

For load variation two scenarios were designed and implemented:

The first case, is titled as "half-step experiment". The changes made in the gas flow rate are as follows: the test starts with the reference point of 21.1 l min^{-1} . After 3 GC runs corresponding to 45 minutes of run time, the total flow rate is reduced to 15.8 l min^{-1} . The reactor response to the step change is monitored for 45 minutes. Thereafter, the flow rate is decreased further to 10.6 l min^{-1} . The same step-change sequence is repeated for altering from 10.6 to 15.8 and afterwards to 21.1 l min^{-1} . The step change is initiated 2 minutes after starting the third GC measurement for the previous condition, in order to make sure that there is enough time for the new adjustments made in the feed can be captured by the GC.

The second scenario deals with the so-called "full-step experiment": The feed flow rate is changed from 21.1 l min^{-1} directly to 10.6 l min^{-1} and back. The time interval for executing the changes is the same as in case of half-step experiment. The results of the full-step scenario are not plotted here, since the same trends were observed in both cases.

In the following, the influence of inducing a step change in flow rate from 21.1

to 15.8 l min^{-1} and the opposite order is discussed in detail. It is beneficial to point out that in this setup all adjustments were done manually. Whereas for
610 an industrial plant the work is being done with an automated control strategy. The temperature map shown in figure 10 is generated using the 5 measurement position along the bed. The profile clarifies the temporal evolution of the temperature throughout the transient conditions. This figure can be divided in 3 sections:

- 615 I. The steady state achieved about 25 minutes after initiating the reaction.
- II. The temperature response to the step change in the feed flow rate and its evolution at $t > 43 \text{ min}$ (switching time).
- III. The new steady-state reached for the new parameter set at around 58 min.

Parallel to temperature map, the water flow rate adjusted to control the sudden
620 temperature changes throughout the time is plotted for better understanding of the involved effects. Fig. 10-left maps the temperature evolution when feed throughput is reduced from 21.1 to 15.8 l min^{-1} . Immediately after the load reduction, the temperature in hotspot (position 2) drops from 440 to $420 \text{ }^\circ\text{C}$. The water mass flow rate is manually reduced to the value derived in the steady-
625 state load change experiment for 15.8 l min^{-1} to prevent further temperature drop. Although the temperature drop stops, the system does not go back to the initial temperature level (hotspot of $440 \text{ }^\circ\text{C}$). Via additional reduction in the coolant amount the temperature starts to grow again and reaches its initial profile. At this point the water flow rate must be readjusted again so that
630 no further temperature increase occurs. The time interval which the reactor requires to adapt to the applied changes and evolve toward its initial stage is about 15-20 minutes.

Fig. 10-right shows the temporal changes in axial temperature for transient conditions of increasing the flow rate from 15.8 to 21.1 l min^{-1} . After inducing
635 the step in the flow rate, a sudden increase of about 10 K is measured in the hot spot. The water flow rate is adjusted instantly in order to avoid temperature runaway. The reactor reacts rather fast to the coolant modification and after about 5 minutes, the temperature starts to diminish. Again, it takes about 15 minutes in total for the reactor to go back to the initial temperature level.
640 During this period also water had to be dosed in over steady-state value for the effective control of the temperature. A maximum increase/decrease of the water flow rate of approximately $1\text{-}2 \text{ g min}^{-1}$ above/below its steady-state values helped in handling the sudden temperature alterations in transient conditions.

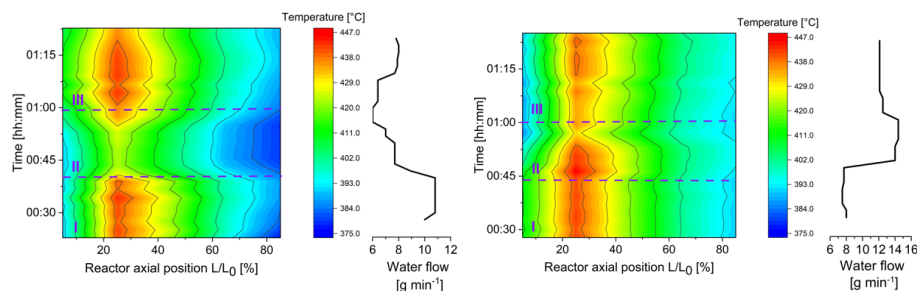


Figure 10: Temperature evolution and the total cooling water flow adjusted during half-step change experiments, left: 21.1 to 15.8 l min^{-1} , right: 15.8 to 21.1 l min^{-1} ($\text{H}_2/\text{CO}_2 = 4$, $p_w = 10$ bar)

The GC measurements shown in figure 11-left signify no deviation from the CO_2 conversion in steady state experiments (section 3.4, table 5). A constant temperature profile in rear reactor part during load changes is reason for constant product quality, as already discussed in section 3.2. Although the GC measurement intervals take long and in an intensive dynamic study, measurement intervals below 5 minutes are desired, we would not expect a dramatic change in the product quality during transient conditions, due to the same argumentation of stable temperature profile of the rear reactor.

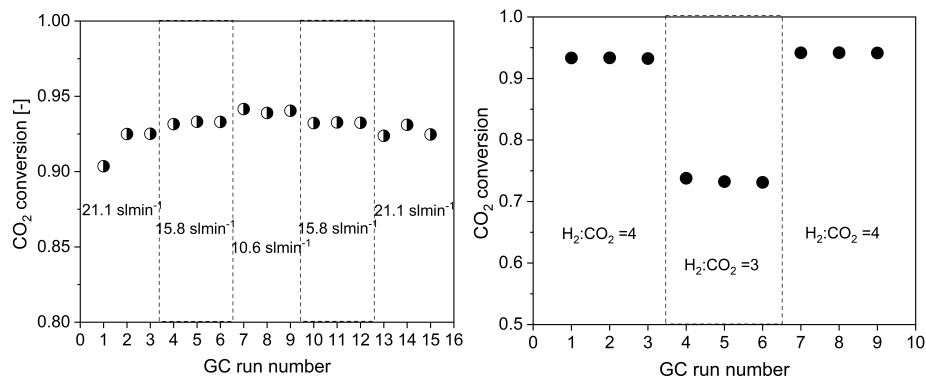


Figure 11: CO_2 conversion and the total cooling water flow adjusted during step change experiment, left: step change in load ($\text{H}_2/\text{CO}_2 = 4$, $p_w = 10$ bar), right: H_2/CO_2 ratio step change ($\dot{V}_{\text{CO}_2} = \text{const.} = 31 \text{ l min}^{-1}$, $p_w = 10$ bar)

3.6.2. H_2/CO_2 step changes

For the case of composition variation, the $\text{H}_2:\text{CO}_2$ ratio is varied from 4 to 3 and back to 4 again. The studied case is applied for the assumption of constant CO_2 flow rate. The same procedure was applied as in the load step variation: each parameter was set for 45 minutes with 3 respective GC runs. The measurement started with H_2/CO_2 ratio of 4 ($\dot{V}_{\text{tot}} = 15.8 \text{ l min}^{-1}$). Figure 12-left shows that the temperature drops 10 K after reducing the H_2 flow rate.

660 With water adjustment (decreasing to 4 g min^{-1}) the temperature in position 2 can be controlled perfectly and it approaches its starting value in less than 10 minutes.

The step change in H_2 flow rate for setting the H_2/CO_2 ratio from 3 to 4 is shown in figure 12-right. Temperature in the hotspot raises to $450 \text{ }^\circ\text{C}$ (10 K increase). In this case also in 10 minutes the perturbations can be counteracted with efficient cooling. Figure 11-right shows the CO_2 conversion throughout the feed composition transient conditions. No fluctuations in the CO_2 conversion is observable, which certifies the stability of the reactor under transient feed compositions.

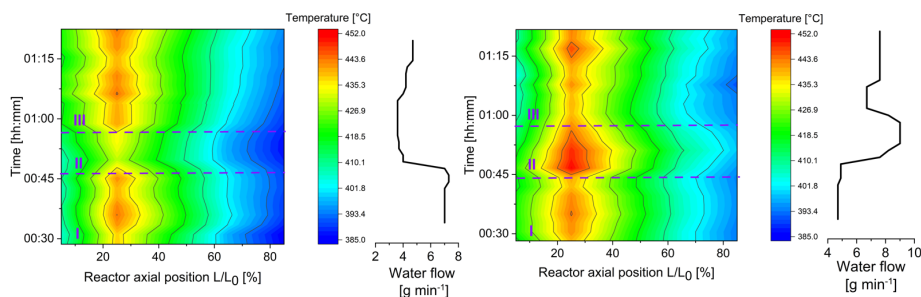


Figure 12: Temperature evolution during H_2/CO_2 step change experiments, left: 4 to 3, right: 3 to 4 ($\dot{V}_{\text{CO}_2} = \text{const.} = 31 \text{ min}^{-1}$, $p_w = 10 \text{ bar}$).

3.7. Modelling of the heat-exchanger reactor

670 The modelling results are briefly discussed for one reference point (P2-test 2, in section 3.2) concerning the temperature and concentration profile. Figure 13 displays the effective heat transfer coefficient (k_{eff}) determined for each CSTR cell and at reference reaction conditions as in experiment (see section 2.3). The heat transfer coefficient in the first CSTR (inlet) is about $75 \text{ W m}^{-2} \text{ K}^{-1}$, which increases sharply to $330 \text{ W m}^{-2} \text{ K}^{-1}$ already in the second cell. The maximum value of k_{eff} reaches $883 \text{ W m}^{-2} \text{ K}^{-1}$ and is located at $L/L_0 = 6\%$. The calculated profile for k_{eff} can be perfectly explained with the nature of evaporation cooling implemented for fast and exothermic methanation. In the first cell, liquid water enters the reactor and reaction is not yet developed either, thus k_{eff} is low. After a short length, the reaction rate increases abruptly and water starts to evaporate, leading to very high k_{eff} values. During evaporation, the vapour fraction grows which leads to gradual reduction of the heat transfer coefficient within some cells. At $L/L_0 = 40\%$, the decreasing slope of k_{eff} changes and increases slightly, likely due to water entering the reactor from the second coolant passage. But since the peak of reaction rate is already passed, the k_{eff} does not change significantly. Afterwards, k_{eff} continues to decline with a small slope to a minimum value of $30 \text{ W m}^{-2} \text{ K}^{-1}$. In this region, steam is superheated. At $L/L_0 = 80\%$, the k_{eff} starts to increase gradually, most probably due to growing heat losses at reactor outlet.

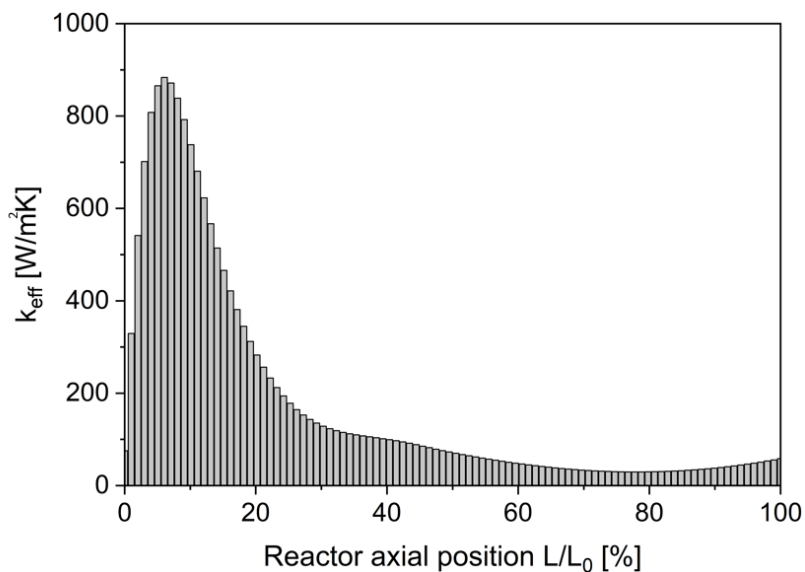


Figure 13: The calculated effective heat transfer coefficient (k_{eff}) for 100 CSTRs along the catalyst bed axis at reference reaction conditions.

690 Figure 14-left depicts the modelled axial temperature profile in the gas phase (reactants), the catalyst surface and catalyst core for the reference case in comparison with the experimental temperature profile. The comparison reveals that the implemented reactor modelling methodology perfectly fits the experimental temperature profile. The position of the hotspot, and the moderate course of temperature decline after the maximum are modelled precisely. As the model
 695 temperature decline after the maximum are modelled precisely. As the model assumptions impose (see section 2.4), the temperature in the catalyst and the gas are identical. The maximum temperature gradient in the catalyst occurs in the reactor front where the kinetics are extremely fast. After $L/L_0 = 30\%$, the intraparticle temperature gradient drops to below 1 K. To conclude, it is confirmed that the reaction is not limited by intraparticle heat transfer.
 700

Modelled CO_2 conversion, CH_4 selectivity and CO yield axial profiles are presented in figure 14-right. CO_2 conversion increases sharply in the temperature increase region; which is approximately the first 20% of the reactor inlet length. After the hotspot, the CO_2 conversion rate is modest. The predicted CO_2 conversion in the outlet is equal to 84% and falls slightly behind the experimentally
 705 measured value.

Since the applied kinetic model describes a consecutive pathway for CO formation, the yield of CO increases shortly in the inlet (max. 8%). At the same location where CO experiences a maximum, the methane selectivity drops. After
 710 this peak, the CO yield declines to 0.4% and the methane selectivity reaches 99.5%. Identical values were measured during experiment for both CO yield and CH_4 selectivity. Therefore, the model provides an accurate prediction on the product distribution.

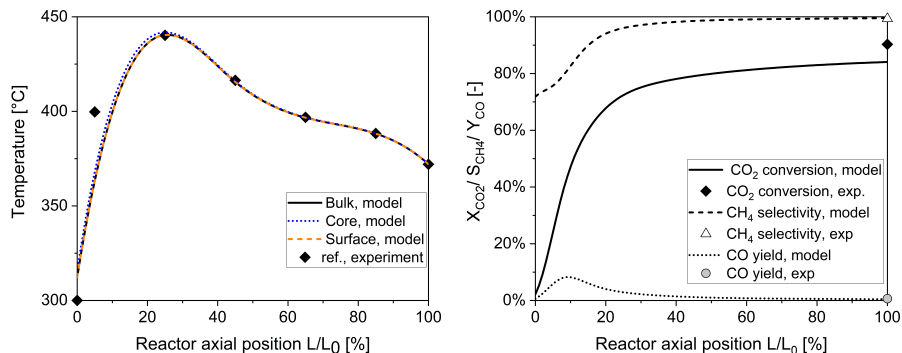


Figure 14: Left: temperature development in the bulk phase, the catalyst core and catalyst surface predicted by the model. Comparison with experimental temperature data for the reference data point. Right: axial CO₂ conversion, CH₄ selectivity and CO yield according to the model and comparison to the experimental data (measured at reactor outlet).

4. Conclusion

715 The application of evaporation cooling for the catalytic methanation reaction of CO₂ and H₂ on a Ni catalyst is investigated in detail. This approach is shown to be highly efficient in the newly developed microstructured heat-exchanger reactor that allows high CO₂ conversion in a single stage. This is highly desired in a PtG process scheme, specially for decentralized applications.

720 The exothermic energy generated through methane formation is perfectly utilized via steam generation, that can be further applied in a steam electrolyzer. The implemented reactor cooling structure is modified compared to the first prototype, examined by Belimov et al. [9], by two cooling inlets. This allows maintaining the enhanced local heat removal and at the same time prevention of

725 reaction blow out caused by excessive cooling. Utilization of pressurized water further promotes an autothermal operation. The reactor has a polytropic temperature profile along the reactor axis and is well-below 500 °C. The hotspot is moderated and can be tuned via smart cooling adjustment, which is accompanied with operational limits in most fixed bed reactors due to parametric

730 sensibility. It was shown that the temperature in different axial positions can be superbly regulated via altering the water distribution in the two passages. The manipulation of the temperature profile via two coolant inlets showed that the hotspot region between 415-455 °C has no influence on CO₂ conversion degree. However, when the temperature in rear reactor part (positions 3-5)

735 is lower than 400 °C, the conversion may be limited by the reaction kinetics. It was also confirmed that the reactor performs stable under a wide range of coolant pressures. However, lower water pressures impose larger temperature fluctuations in the catalyst bed.

740 A wide range of reaction throughput and compositions were studied that endorsed promising reactor performance under the tested conditions. Finally, the temperature profile evolution and product perturbation under transient load

and feed composition were monitored. The step changes showed that under transient conditions in the inlet feed flow rate, the reactor requires maximum 30 minutes for re-stabilization and regulating towards its initial temperature level with minimal coolant flow changes. No changes in the products quality was measured under the performed step change experiments.

For numerical diagnosis of the used reactor, a 1D heterogeneous model with 100 CSTR cells was applied in Matlab. The heat transfer coefficient was calculated for each CSTR cell through a fit of the axial temperature profile from experimental data. The axial heat transfer coefficient provided valuable information on the progression of evaporation. Comparison to the experimental data showed that the developed model can predict the concentration in the output and the axial temperature profile precisely.

The insights achieved from this reactor have been applied for the scale-up (scale-up factor= 28) and validation of a modular reactor technology for 100 kW methane generation. The scaled-up microstructured reactor prototype has been implemented in a pilot plant in the Energy Lab 2.0. In this respect, application of the evaporation cooling for the methanation micro-reactor for $10 \text{ m}^3 \text{ h}^{-1}$ methane generation is validated [36].

Acknowledgment

Funding of this research by the German Ministry for Education and Research (BMBF) within the KOPERNIKUS Project Power2X (P2X) under contract No. 03SFK2K0 is gratefully acknowledged.

The authors sincerely appreciate the support of INERATEC GmbH for providing the Ni catalyst applied in this study and the fruitful cooperation.

References

References

- [1] NASA, The effects of climate change (2020).
URL <https://climate.nasa.gov/effects/>
- [2] N. Nuttall, Historic paris agreement on climate change: 195 nations set path to keep temperature rise well below 2 degrees celsius (13.12.2015).
URL <https://unfccc.int/news/finale-cop21>
- [3] M. Sterner, I. Stadler, Energiespeicher - Bedarf, Technologien, Integration, Springer Berlin Heidelberg, Berlin, Heidelberg, 2017. doi:10.1007/978-3-662-48893-5.
- [4] Hydrogen power storage & solutions east Germany (2020). [link].
URL <https://www.hypos-eastgermany.de/das-innovationsprojekt/hypos-strategie/>

- 780 [5] M. Götz, J. Lefebvre, F. Mörs, A. McDaniel Koch, F. Graf, S. Bajohr, R. Reimert, T. Kolb, Renewable power-to-gas: A technological and economic review, *Renewable Energy* 85 (2016) 1371–1390. doi:10.1016/j.renene.2015.07.066.
- [6] S. Rönsch, J. Schneider, S. Matthischke, M. Schlüter, M. Götz, J. Lefebvre, P. Prabhakaran, S. Bajohr, Review on methanation – from fundamentals to current projects, *Fuel* 166 (2016) 276–296. doi:10.1016/j.fuel.2015.10.111.
- 785 [7] M. Bailera, P. Lisbona, L. M. Romeo, S. Espatolero, Power to gas projects review: Lab, pilot and demo plants for storing renewable energy and co₂, *Renewable and Sustainable Energy Reviews* 69 (2017) 292–312. doi:10.1016/j.rser.2016.11.130.
- 790 [8] J. Gao, Y. Wang, Y. Ping, D. Hu, G. Xu, F. Gu, F. Su, A thermodynamic analysis of methanation reactions of carbon oxides for the production of synthetic natural gas, *RSC Advances* 2 (6) (2012) 2358. doi:10.1039/c2ra00632d.
- [9] M. Belimov, D. Metzger, P. Pfeifer, On the temperature control in a microstructured packed bed reactor for methanation of co/co₂ mixtures, *AIChE Journal* 63 (1) (2017) 120–129. doi:10.1002/aic.15461.
- 795 [10] J. H. Jensen, J. M. Poulsen, N. U. Andersen, From coal to clean energy, *Nitrogen+Syngas* 310 (2011) 34–38.
- [11] Jan Kopyscinski, Production of synthetic natural gas in a fluidized bed reactor: Understanding the hydrodynamic, mass transfer, and kinetic effects, ETH Zurich, Zurich, 2010.
- 800 [12] D. Schollenberger, S. Bajohr, M. Gruber, R. Reimert, T. Kolb, Scale-up of innovative honeycomb reactors for power-to-gas applications - the project store&go, *Chemie-ingenieur-technik* 90 (5) (2018) 696–702. doi:10.1002/cite.201700139.
- [13] S. Razza, T. Heidig, E. Bianchi, G. Groppi, W. Schwieger, E. Tronconi, H. Freund, Heat transfer performance of structured catalytic reactors packed with metal foam supports: Influence of wall coupling, *Catalysis Today* 273 (2016) 187–195. doi:10.1016/j.cattod.2016.02.058.
- 810 [14] Y. Li, Q. Zhang, R. Chai, G. Zhao, F. Cao, Y. Liu, Y. Lu, Metal-foam-structured ni-al₂o₃ catalysts: Wet chemical etching preparation and syngas methanation performance, *Applied Catalysis A: General* 510 (2016) 216–226. doi:10.1016/j.apcata.2015.11.034.
- [15] N. Engelbrecht, S. Chiuta, R. C. Everson, H. W. Neomagus, D. G. Bessarabov, Experimentation and cfd modelling of a microchannel reactor for carbon dioxide methanation, *Chemical Engineering Journal* 313 (2017) 847–857. doi:10.1016/j.cej.2016.10.131.
- 815

- [16] K. P. Brooks, J. Hu, H. Zhu, R. J. Kee, Methanation of carbon dioxide by hydrogen reduction using the sabatier process in microchannel reactors, *Chemical Engineering Science* 62 (4) (2007) 1161–1170. doi:10.1016/j.ces.2006.11.020.
- [17] O. Görke, P. Pfeifer, K. Schubert, Highly selective methanation by the use of a microchannel reactor, *Catalysis Today* 110 (1-2) (2005) 132–139. doi:10.1016/j.cattod.2005.09.009.
- [18] Z. Liu, B. Chu, X. Zhai, Y. Jin, Y. Cheng, Total methanation of syngas to synthetic natural gas over ni catalyst in a micro-channel reactor, *Fuel* 95 (2012) 599–605. doi:10.1016/j.fuel.2011.12.045.
- [19] Michael Neubert, Alexander Hauser, Babak Pourhossein, Marius Dillig, Juergen Karl, Experimental evaluation of a heat pipe cooled structured reactor as part of a two-stage catalytic methanation process in power-to-gas applications, *Applied Energy* 229 (2018) 289–298. doi:10.1016/j.apenergy.2018.08.002.
URL <http://www.sciencedirect.com/science/article/pii/S0306261918311577>
- [20] A. Alarcón, J. Guilera, T. Andreu, Co2 conversion to synthetic natural gas: Reactor design over ni-ce/al2o3 catalyst, *Chemical Engineering Research and Design* 140 (2018) 155–165. doi:10.1016/j.cherd.2018.10.017.
URL <http://www.sciencedirect.com/science/article/pii/S0263876218305392>
- [21] E. Giglio, F. A. Deorsola, M. Gruber, S. R. Harth, E. A. Morosanu, D. Trimis, S. Bensaid, R. Pirone, Power-to-gas through high temperature electrolysis and carbon dioxide methanation: Reactor design and process modeling, *Industrial & Engineering Chemistry Research* 57 (11) (2018) 4007–4018. doi:10.1021/acs.iecr.8b00477.
- [22] J. Bremer, K. H. G. Rätze, K. Sundmacher, Co2 methanation: Optimal start-up control of a fixed-bed reactor for power-to-gas applications, *AIChE Journal* 63 (1) (2017) 23–31. doi:10.1002/aic.15496.
- [23] A. El Sibai, L. K. Rihko Struckmann, K. Sundmacher, Model-based optimal sabatier reactor design for power-to-gas applications, *Energy Technology* 5 (6) (2017) 911–921. doi:10.1002/ente.201600600.
- [24] R. Güttel, Study of unsteady-state operation of methanation by modeling and simulation, *Chemical Engineering & Technology* 83 (11) (2013) n/a–n/a. doi:10.1002/ceat.201300223.
- [25] X. Li, B. Yang, Y. Zhang, Dynamics and control study on the low temperature methanation reactor with mass and heat recycle, *Journal of Process Control* 23 (10) (2013) 1360–1370. doi:10.1016/j.jprocont.2013.09.003.

- [26] K. L. Fischer, H. Freund, On the optimal design of load flexible fixed bed reactors: Integration of dynamics into the design problem, *Chemical Engineering Journal* 393 (2020) 124722. doi:10.1016/j.cej.2020.124722. URL <http://www.sciencedirect.com/science/article/pii/S1385894720307130>
- [27] S. Matthischke, R. Krüger, S. Rönsch, R. Güttel, Unsteady-state methanation of carbon dioxide in a fixed-bed recycle reactor — experimental results for transient flow rate ramps, *Fuel Processing Technology* 153 (2016) 87–93. doi:10.1016/j.fuproc.2016.07.021.
- [28] Jonathan Lefebvre, Manuel Götz, Siegfried Bajohr, Rainer Reimert, Thomas Kolb, Improvement of three-phase methanation reactor performance for steady-state and transient operation, *Fuel Processing Technology* 132 (2015) 83–90. doi:10.1016/j.fuproc.2014.10.040. URL <http://www.sciencedirect.com/science/article/pii/S0378382014004640>
- [29] M. N. Kashid, A. Renken, L. Kiwi-Minsker, *Microstructured devices for chemical processing*, Wiley-VCH, Weinheim, 2015.
- [30] P. Pfeifer, M. Belimov, *Microreactor and process control for methanation: Microreactors, e.g. miniaturised or microfabricated reactors* (2017). URL <https://patents.google.com/patent/DE102016110498A1/en>
- [31] J. Guilera, T. Boeltken, F. Timm, I. Mallol, A. Alarcón, T. Andreu, Pushing the limits of sng process intensification: High gHSV operation at pilot scale, *ACS Sustainable Chemistry & Engineering* 8 (22) (2020) 8409–8418. doi:10.1021/acssuschemeng.0c02642.
- [32] S. Farsi, W. Olbrich, P. Pfeifer, R. Dittmeyer, A consecutive methanation scheme for conversion of CO₂ – a study on Ni₃Fe catalyst in a short-contact time micro packed bed reactor, *Chemical Engineering Journal* 388 (2020) 124233. doi:10.1016/j.cej.2020.124233.
- [33] M. Belimov, Methane production from co-electrolysis products applying a microchannel reactor. doi:10.5445/IR/1000126562.
- [34] R. Dittmeyer, G. Emig, Simultaneous heat and mass transfer and chemical reaction, in: G. Ertl (Ed.), *Handbook of heterogeneous catalysis*, Wiley-VCH, Weinheim and Chichester, 2008. doi:10.1002/9783527610044.hetcat0094.
- [35] M. Baerns, H. Hofmann, A. Renken (Eds.), *Lehrbuch der technischen Chemie*, 2nd Edition, Thieme, Stuttgart, 1992.
- [36] Karlsruhe Institute of Technology, <https://www.elab2.kit.edu/> (2018).